JOURNAL OF PROPULSION AND POWER
Vol. 17, No. 3, May–June 2001

Laser Doppler Anemometry Measurements in an Axial Compressor Stage

Thierry M. Faure,* Guy-Jean Michon,† Hubert Miton,‡ and Nicolas Vassilieff§
Université Pierre et Marie Curie, Paris 6, 91405 Orsay, France

The aim is to provide unsteady experimental data of the flowfield in a benchmark one-stage axial compressor, to improve the understanding of the flow features. The investigation is conducted with a two-component laser Doppler anemometer, and 32 axial locations are surveyed, from the rotor inlet to the stator outlet. Because laser Doppler anemometry is a nonintrusive device, data are obtained from the rotor row, providing information in a region difficult to explore with other techniques. Limitation of blade shadowing is addressed with an adjustment of the laser head orientation, which permits reaching any point inside the rotor. Furthermore, a dual probe orientation gives two sets of measurements yielding three velocity components. The dynamics of the rotor tip clearance vortex is discussed in the interrow gap. There is a strong interaction between this vortex and the rotor blade wake. Phase-averaged results show the unsteady flowfield and the rotor–stator interaction. The rotor wakes are cut up by the stator row and are visible until the exit of the axial zone of measurements. Their interaction with the stator blades boundary layers creates strong time-dependent flow structures resulting in phase lags between the rotor wakes at the stator outlet.

Nomenclature

A_{ij}	=	matrix (4 × 3) of geometrical probe volume position
c_r	=	rotor blade axial chord at midspan
D	=	determinant
H	=	normalized distance between the hub and the casing
N	=	parameter of geometrical probe volume position
p_{t_1}	=	inlet total pressure
p_{t_2}	=	outlet total pressure
r	=	radial direction
r_h	=	hub radius
r_t	=	tip radius
t	=	time
V	=	absolute velocity
W	=	relative velocity
x	=	axial direction
α	=	absolute angle
β	=	relative angle
θ	=	tangential direction
ϑ	=	laser head pitch angle
φ	=	laser head roll angle
ϕ	=	phase angle
ψ	=	laser head yaw angle

Subscripts

b	=	blue laser component
g	=	green laser component
i	=	index
m	=	meridian component
x, r, θ	=	axial, radial, and tangential directions
1	=	first laser head position
2	=	second laser head position

Superscript

$\sim$	=	phase-averaged property

Received 15 November 1999; revision received 30 June 2000; accepted for publication 10 July 2000.

*Assistant Professor, Laboratoire d'Énergétique et de Mécanique des Fluides Interne. Member AIAA.
†Research Engineer, Laboratoire d'Énergétique et de Mécanique des Fluides Interne.
‡Researcher, Laboratoire d'Énergétique et de Mécanique des Fluides Interne.
§Research Assistant, Laboratoire d'Énergétique et de Mécanique des Fluides Interne.

I. Introduction

RECENT improvements in axial turbomachinery lead to a compressor efficiency that tends to an asymptotic value. Nowadays, the need is not only to understand the behavior of the mean flowfield, but also to get information on the time-dependent features. For a better understanding of the unsteady velocity, inside a confined high-velocity rotating channel, it is necessary to use unsteady and nonintrusive measurement systems.

Thus, laser velocimetry is a useful tool for turbomachinery flow investigation, which is able to provide information on the three-dimensional velocity field. Some attempts to use laser two focus (L2F) anemometers have been carried out[1–3] in this kind of high-loaded, high-speed rotating flow. The extension of these systems for three-dimensional measurements are under development.[4–8] However, L2F anemometry measurements are difficult to validate for complex and turbulent three-dimensional high-speed flows. That is the reason we preferred using laser Doppler anemometry (LDA) for this study. Furthermore, this technique is still evolving. The miniaturization of hardware, with recent improvements in laser diodes and photodiodes, will lead in the near future to miniature systems at a low cost.[9] These new systems tend to improve the resolution of the probe volume or to measure the spatial turbulence correlation.[10] Additional improvements are made in the signal processing of the electric output of the photomultiplier. In the past, the common technique was to count the zero crossing of the Doppler signal; however, now, the spectral analysis of Doppler bursts is preferred. This is a much more powerful technique and can operate in high background noise conditions.[11]

Most of the recent work on unsteady three-dimensional flow in turbomachinery has been conducted in rotor turbines.[12–15] The first application of a three-component LDA on an axial-flow compressor, was carried out by Chesnakas and Dancey.[16] However, the experiments performed in compressor rigs are usually limited to turbulence measurements within the airfoil rows[17] or tip leakage studies. For instance, Murthy and Lakshminarayana[18] made LDA two-component measurements of the tip region flowfield within and aft of the axial compressor blade passage. Stauter[19] used a five-beam LDA system to make time-resolved measurements both between compressor blade rows and within the rotating blade passages in an axial compressor, to track the three-dimensional flow in the tip region.

In the present investigation, a two-component, two-color LDA is implemented to explore the flow inside a compressor stage. Measurements are completed inside the rotor and stator, providing flow characteristics in regions difficult to investigate with other techniques. The use of the laser head with two off-axis orientations yields the three components of velocity. Time-dependent averages are processed in phase with rotor position to analyze the unsteady flow behavior.

II. Experimental Facility and Instrumentation

A. Test Rig

The single-stage axial compressor setup (CME2) of the laboratory is shown in Fig. 1. This open-circuit facility consists of an inlet with filters for the atmospheric air, a settling chamber followed by the compressor test rig, a flow adjuster, and an outlet duct discharging in the room. This is an improvement of a testbed used for unsteady hot-wire interrow investigation of a four-stage axial compressor.[20–23] The compressor stage is fitted with a 30-blade rotor and a 40-blade stator. The axial length of the test section is 180 mm, and the radius of the casing $r_t = 275$ mm. The blade clearance is 0.5 mm in the rotor. The hub radius r_h is increasing from 207 mm in rotor inlet to 212.1 mm in rotor oulet and is constant inside the stator row. A summary of the blade geometry is given in Tables 1 and 2. The origin of the axial coordinate is located near the leading edge of the rotor blade hub.

The rotor is powered by an electrical driving motor that delivers a maximum of 180 kW. It drives a low-speed shaft, so that rotor speed is increased by a multiplier to a high-speed shaft, the high-speed/low-speed ratio being 2.345. At the operating point and for standard conditions (inlet temperature 15°C and pressure 101,325 Pa), the speed of rotation is fixed to 6330 ± 14 rpm, and the flow rate is 10.5 ± 0.1 kg/s, providing a total pressure ratio $p_{t_2}/p_{t_1} = 1.15$. The flow rate can be regulated by axial displacement of the hub wall downstream of the compressor rig outlet. This wall is driven by an electrical dc motor controlled by a personal computer. Inlet and outlet temperatures are obtained from platinium resistance gauges introduced radially in the compressor, as well as total pressure probes to estimate the compressor pressure ratio. The instantaneous blade position is obtained by an optical shaft encoder that delivers a periodic 0–5 V amplitude signal per revolution. This signal is recorded and used in post-processing to calculate phase-averaged velocities.

Table 1 Rotor blade geometry

Span	Chord, mm	Thickness, mm	Stagger angle, deg	Camber angle, deg
Hub	84	7.9	33.5	41.5
Midspan	84	5.6	46	23
Tip	84	2.8	54	20

Table 2 Stator blade geometry

Span	Chord, mm	Thickness, mm	Stagger angle, deg	Camber angle, deg
Hub	77	6.2	17.5	46.5
Midspan	77	6.2	15	41.5
Tip	77	6.2	12.5	36

B. LDA System

The laser Doppler anemometer is a Dantec two-color, four-beam, two-dimensional measuring system. The source is a 5-W argon-ion laser (Coherent model Innova 305) tuned to the 488 nm (blue) and 514.5 nm (green) wavelengths. A power tracking system ensures time stability of laser light emission, whose intensity is a Gaussian-like profile. Each color beam is split in two, and one of these is passed through a 40-MHz Bragg cell, where it is frequency shifted to reduce fringe bias and to solve the direction ambiguity. The half-angle of the beams is 6.772 deg and the measuring volume is 0.8 mm in length and 0.1 mm in diameter. The laser focal distance is 160 mm. Scattered light from the seeding particles passing through the probe volume is collected off-axis from the test rig, which means the optical axis is not aligned with the radial axis. Such an orientation permits closer approach to the access window with the probe volume. The hub and rotor and stator blades are black anodized to reduce surface light reflexions.

In this experiment, because the compressor stage is included in an open-circuit facility, liquid seeding material is preferred. It is provided by a fog created by a fluid containing glycerol, heated and atomized by a SAFEX 2001 smoke generator. The main advantages of this flow-seeding material are its low cost and its easy use. Furthermore, it provides few deposits on the window and the blades, in comparison with oil or incense. Because many points of measurements are recorded per axial section and a long measurement time is necessary to complete a grid section, deposits can affect the window and drastically decrease or stop the data acquisition rate. A cleaning system that removes periodically any dust on the window, without stopping the compressor and removing the window frame, which is an operation that is time consuming, was developed to address this issue. This cleaning system consists of a water and soap mixture injected at two locations on the window frame, providing cleaning for the complete window surface. The seeding fluid is atomized and introduced in the settling chamber 20 cm before the section contraction. According to the seeding fluid manufacturer, the average particle diameter is 1.068 μm, and the particle density is 10^3 kg/m^3.

To explore the blade to blade channel, the laser head, which is used both for the laser light emission and backscattered light collection, is mounted on a manipulation robot. This six-degree-of-freedom arm permits the measurement volume to reach any part inside the compressor. The construction of the three-dimensional field requires two measurements at the same place but with different azimuth angular positions. This assumes more than three degree of freedom. The system enables very accurate positioning: The repeatability for

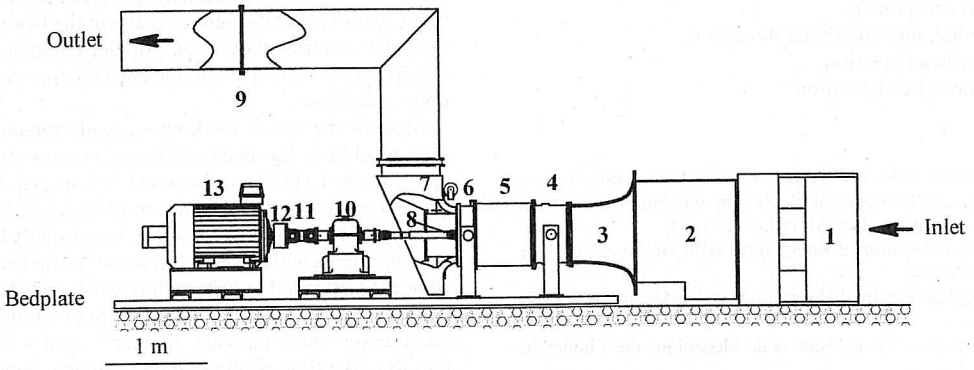

Fig. 1 Experimental setup: 1) inlet filters, 2) settling chamber, 3) convergent, 4) forward bearing, 5) compressor stage, 6) aft bearing, 7) mass flow adjuster, 8) high-speed cardan, 9) diaphragm, 10) multiplier, 11) low-speed cardan, 12) torque limiter, and 13) driving motor (180 kW).

the measurement volume location is around 20 μm. Furthermore, the cost of this system is no higher than a high-precision controlled traverse and offers many possibilities for future experiments. No experimental problem was found in conducting measurements, except near the rotor hub inlet and the access window.

The flow in the compressor stage is measured through a curved Plexiglas® rectangular window, which is 200 mm in length and 136 mm wide. It is 2 mm thick, conforming to the cylindrical shape of the casing.

To run the probe displacements, record and process data, a Hewlett Packard workstation is interfaced through an Institute of Electrical and Electronics Engineers connection to the Dantec burst signal analyzers (BSA), which are 14-bit data samplers.[24] The analyzers use a hardware fast Fourier transform to measure and to validate the backscattered signal at up to 10,000 bursts per second. The two components are not taken in coincidence filtering, and the number of validated bursts per measurement point is 3000, providing for a confidence level of 95% and error of 0.72% in mean velocity, by the use of the method employed by Strazisar.[25] In addition, the laser head displacements are controlled through an RS232 connection. A program has been developped for this study, its main characteristics are as follows.

1) In the first in/first out mode, for each BSA the buffer data are transferred to the workstation during data acquisition.

2) Acquisition is possible with one, two, or three BSA.

3) There is automatic recording of acquisition parameters such as the BSA's setup, position in the robot frame, position in the compressor frame, laser power, etc.

4) There is real-time control with automatic display of data histograms concerning the current measurement point.

To access the phase ϕ (the arrival time of a Doppler burst, related to a blade rotor passage), a top-turn system has been developed. Its principle is to provide a top signal for each rotor rotation; hence, the blade crossing time is deduced. This top-turn signal is recorded with the output of one BSA. Afterward, the phase of a measurement is found with

$$\phi = \frac{t - t_i}{t_{i+1} - t_i}$$

where t_i and t_{i+1} are the crossing times for blades i and $i+1$ before and after the particle arrival time, respectively. This method is very accurate because the rotation can be assumed constant during a revolution.

C. LDA Data Reduction

In this study, 32 axial sections, spreading from the compressor inlet to the outlet are surveyed. For each plane, 224 measurement points are recorded, covering a blade to blade, hub to tip channel. The problem of the passage of the rotor blades through the incident beams can reduce the investigation zone. It is corrected by the use of an azimutal position of the laser head axis, which is adapted to the region the probe volume should reach. Thus the limitation of blade shadowing is addressed. Furthermore, the three-dimensional velocity field can be obtained by the implementation of two laser head orientations per point of measurement, leading to two sets of two different velocity components. Because of the high-speed application and the use of BSA, no blade flash problem occurred for particle detection; the light scattered by the blade was detected and rejected by the analyzers. The laser head is mounted on the arm of the manipulation robot (Fig. 2). A frame of reference for the head axis is defined relative to the compressor frame of reference by the angles ϑ, ψ, and φ, respectively, of the pitch, yaw, and roll angle with the head axis direction (Fig. 3). The two positions are defined by two sets of angular parameters, $(\vartheta_1, \psi_1, \varphi_1)$ and $(\vartheta_2, \psi_2, \varphi_2)$, respectively, with $\psi_1 = -10$ deg and $\psi_2 = 10$ deg. If there is no problem of accessibility of the probe volume inside blades and walls, then $\vartheta_1 = \theta_1 = \theta_2 = \vartheta_2$ and $\varphi_1 = \varphi_2$; otherwise these values are corrected by a masking program. In the first position, two velocity components V_{b_1} and V_{g_1} relative to the blue and green laser beams are measured, and the second position leads to another set of velocities

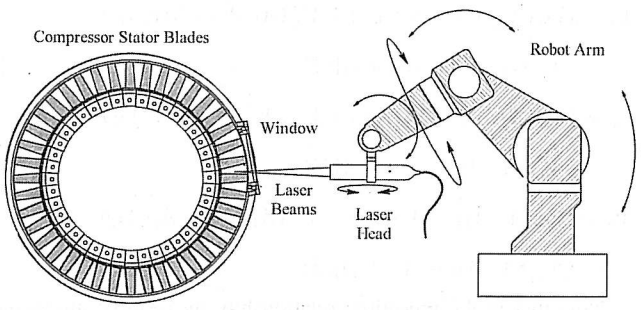

Fig. 2 Robot arm with laser head and optical access to compressor.

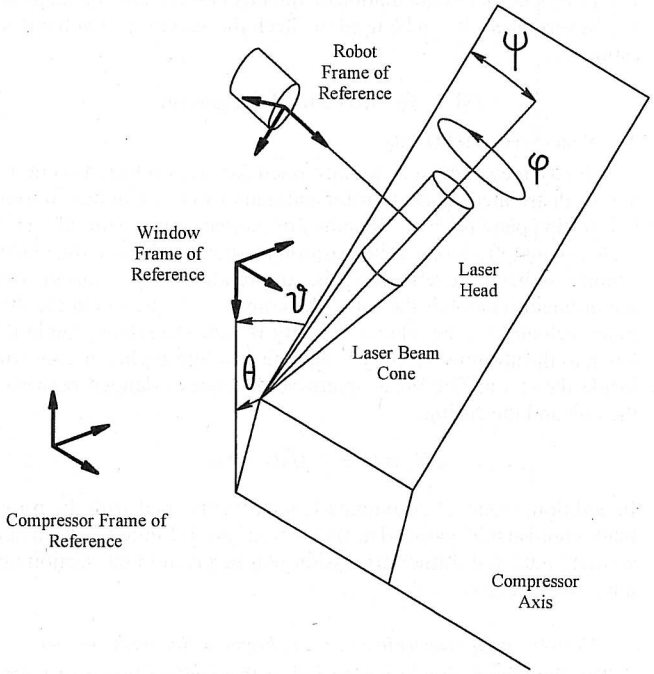

Fig. 3 Laser head angles relative to compressor frame of reference.

V_{b_2} and V_{g_2}. Let us define the parameters of the geometrical laser head position, relative to the compressor coordinates x, r, and θ:

$$N_{b_x} = \cos\psi \cos(\varphi - \pi/4)$$

$$N_{b_r} = \cos\vartheta \sin\psi \cos(\varphi - \pi/4) - \sin\vartheta \sin(\varphi - \pi/4)$$

$$N_{b_\theta} = -\cos\vartheta \sin(\varphi - \pi/4) - \sin\vartheta \sin\psi \cos(\varphi - \pi/4)$$

$$N_{g_x} = \cos\psi \cos(\varphi + \pi/4)$$

$$N_{g_r} = \cos\vartheta \sin\psi \cos(\varphi + \pi/4) - \sin\vartheta \sin(\varphi + \pi/4)$$

$$N_{g_\theta} = -\cos\vartheta \sin(\varphi + \pi/4) - \sin\vartheta \sin\psi \cos(\varphi + \pi/4)$$

These parameters are part of a 4×3 matrix A_{ij} with

$$A_{11} = N_{b_{x_1}}, \quad A_{12} = N_{b_{r_1}}, \quad A_{13} = N_{b_{\theta_1}}$$

$$A_{21} = N_{b_{x_2}}, \quad A_{22} = N_{b_{r_2}}, \quad A_{23} = N_{b_{\theta_2}}$$

$$A_{31} = N_{g_{x_1}}, \quad A_{32} = N_{g_{r_1}}, \quad A_{33} = N_{g_{\theta_1}}$$

$$A_{41} = N_{g_{x_2}}, \quad A_{42} = N_{g_{r_2}}, \quad A_{43} = N_{g_{\theta_2}}$$

The determinant of the three first lines of this matrix is

$$D = A_{11}(A_{22}A_{33} - A_{32}A_{23}) - A_{21}(A_{12}A_{33} - A_{32}A_{13}) + A_{31}(A_{12}A_{23} - A_{22}A_{13})$$

Then, the three components of velocity in a cylindrical frame of reference attached to the compressor are calculated:

$$V_x = [V_{b_1}(A_{22}A_{33} - A_{32}A_{23}) + V_{b_2}(A_{13}A_{32} - A_{33}A_{12}) + V_{g_1}(A_{12}A_{23} - A_{13}A_{22})]/D$$

$$V_r = [V_{b_1}(A_{23}A_{31} - A_{21}A_{33}) + V_{b_2}(A_{11}A_{33} - A_{13}A_{31}) + V_{g_1}(A_{13}A_{21} - A_{11}A_{23})]/D$$

$$V_\theta = [V_{b_1}(A_{21}A_{32} - A_{22}A_{31}) + V_{b_2}(A_{12}A_{31} - A_{11}A_{32}) + V_{g_1}(A_{11}A_{22} - A_{12}A_{21})]/D$$

Note that in the preceding relationship, the velocity measured from the green laser beam, with the second laser head orientation V_{g_2}, is useless for the calculation of velocity components V_x, V_r, and V_θ. Nevertheless, it can be used to check the accuracy of velocities estimates.

III. Results and Discussion

A. Time-Averaged Velocity

Velocity measurements are discussed for eight selected sections axially distributed inside the rotor and stator rows and for five chosen hub to tip spanwise radii. Results are plotted vs the azimuth: The scales change from one axial position to another because the blade channel is bent. Nevertheless, the amplitude is kept constant for the ordinate scale. For the rotor, the components presented are the radial velocity V_r, the relative velocity W, and the relative angle β, whereas the absolute velocity V and the absolute angle α are shown inside the stator. The blade spanwise distance is defined between the hub and the casing:

$$H = (r - r_h)/(r_t - r_h)$$

In addition, the axial coordinate is nondimensioned with the rotor blade chord at midspan c_r. The present analysis is limited to the mean velocity field and further discussion will be given in the section on unsteady velocity.

1. Time-Averaged Velocity in a Rotating Frame of Reference (Rotor)

The time averaging is performed in the relative frame of reference, rotating with the rotor blades. These averages are carried out to remove any turbulent part in the velocity signal. Figure 4 shows the distribution over a blade to blade azimuth of the averaged radial velocity V_r in a rotating frame of reference, upstream, inside, and immediately downstream of the rotor row. Note that all of the profiles for $H = 22\%$ span are a little jagged because of greater measurement uncertainties due to the difficulty of introducing proper seeding in that zone and the important noise in the scattered light. For these reasons, results for lower spans inside the rotor row are not shown. The V_r velocity component is difficult to obtain, but it is small compared with axial and tangential velocities. However, it is taken into account for the estimates of W or V. The main variations of V_r are observed at the rotor outlet in the blade wakes. The averaged relative velocity distribution is shown in Fig. 5. For the first plane, located at $x/c_r = -0.059$, the potential blockage of the rotor blade causes a smooth depression in the velocity profile for every spanwise location. We also notice the regular velocity increase with span, caused by a greater entrainment velocity at the blade tip. Because of the increase of the stagger angle of the rotor blade from the hub to the tip, this first measurement plane is farther away from the leading edge for the $H = 90\%$ span than for the $H = 22\%$ span. For $x/c_r = 0.12$, a plane inside the rotor channel, the relative velocity distribution increases linearly from the pressure side to the suction side. For the span corresponding to $H = 22\%$, the distribution is not as linear because of lower acquisition data rates. The plane $x/c_r = 0.63$ shows an almost constant distribution from the pressure side to the suction side: This plane of measurement is located slightly before the rotor exit. For the rotor outlet ($x/c_r = 0.80$), the velocity distribution is flat out of the blade wake, which is noticeable as a velocity depression. The wider wake region for the $H = 90\%$ span is certainly due to a tip clearance vortex. This vortex is created on the blade suction side because of the pressure gradient and is convected downstream. After the blade trailing edge, the vortex is deflected by interaction with the wake and is detected on the wake side corresponding to the blade pressure side.

2. Time-Averaged Velocity in a Fixed Frame of Reference (Stator)

Figure 6 shows the absolute velocity distribution V inside the stator row. The flow is decelerated between the inlet and the outlet of the row, from a 130 m/s maximum value to 100 m/s, as the stator plays its role by converting velocity into pressure. For the inlet location ($x/c_r = 0.93$), the velocity gradient is higher at the suction side, and the blockage due to the leading edge of the blade can be identified as velocity minima. The linear velocity increase from the pressure side to the suction side is clearly observed inside the stator channel for $x/c_r = 1.23$. However this velocity gradient is smoothed by the channel camber as long as the flow goes to the stator outlet, providing an almost constant velocity distribution at $x/c_r = 1.87$ except in the blade wakes. Figure 7 shows the distribution of the absolute angle α inside the stator. We notice that the order in magnitude of this quantity decreases from around 45 deg at the inlet to 0 deg at the outlet; this shows the stator row influence on the axial orientation of the flow. For the plane at $x/c_r = 0.93$, the large variations of α (around 10 deg) are associated with the blockage effect at the blade leading edge. Note the tangential variation of the absolute angle α with radius, which varies from 10 deg for $H = 22\%$ to 20 deg for $H = 90\%$. This can be explained by the rotor blade camber difference between the hub and the tip. For $x/c_r = 1.23$, the absolute flow angle α is quite uniform between the suction and pressure sides and disturbed only near the blade trailing edge ($x/c_r = 1.74$) because of the increase of the boundary layers. At the exit, the stator wake causes a small decrease of absolute angle at the suction side (−5 deg) and, as a consequence, a small increase at the pressure side (5 deg).

B. Unsteady Velocity

The periodic part of the flow motion relative to the compressor rotation is discussed in this section. Phase-averaged data are calculated from the time-dependent velocity signals delivered by the BSA thanks to the synchronization top-turn signal. The period of the top-turn signal is 9.48×10^{-3} s. Because the rotor blade number is 30, this gives a blade to blade passing period of 3.16×10^{-4} s. The interblade rotor channel is divided into 24 time-dependent positions providing a time step $\Delta t = 1.32 \times 10^{-5}$ s and an accuracy of 0.5 deg for the description of flow structures. Although the unsteady phenomena are split into 24 phases, only 6 are shown for an easier understanding of periodic flow motion. Figure 8 is a three-dimensional view of the investigated region covering rotor inlet to stator outlet with the time-dependent blade positions. The axial absolute velocity is shown for three orthogonal sections to visualize the different levels inside the compressor stage: 1) an inlet–outlet, root-tip section, referred to as section A, situated at 25% of the stator blade passage width; 2) a stator blade to blade section (r, θ plane) situated in the rotor–stator gap at $x/c_r = 0.87$ and referred to as section B; and 3) a section at a constant $H = 31\%$ (x, θ plane), referred to as section C.

Note that section A is a rectangular plane inside the rotor row (x, r plane) and is a curved surface conforming to the blade suction side inside the stator row. A large blue region inside the stator in section A, without any periodic change, is associated to flow acceleration on the stator blade. It is visible for every phase. The red stripes at the top of sections A and B are the casing boundary layers that spread from the inlet to the outlet. The blade rotor wake is clearly identified in section B as a time-dependent yellow zone associated to a velocity defect close to 65 m/s. In addition, the red time-dependent region at the tip of the blade corresponds to the low-velocity core of the tip clearance vortex. This vortex is strong for phases 1 and 5 and tends to vanish when it is convected by the mean axial flow. Also, the rotor blade blockage effect resulting in a lower yellow velocity zone immediately at the rotor blade leading edge in section C can be observed in Fig. 8

In Fig. 9, the axial velocity is detailed for three planes of measurements, situated in the rotor inlet ($x/c_r = -0.059$), rotor–stator gap

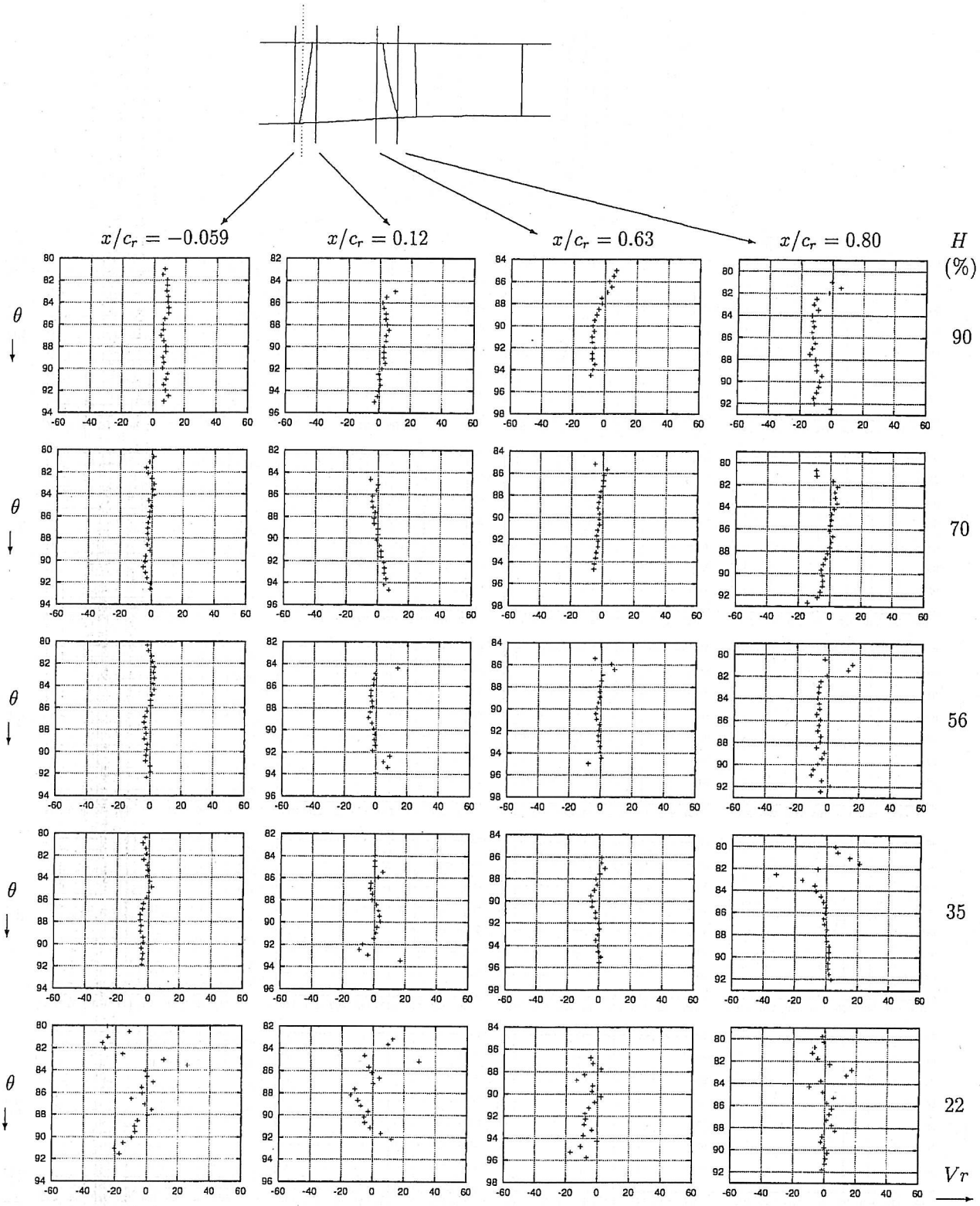

Fig. 4 Tangential distribution (degree) of the radial velocity V_r (m/s) in the rotating frame of reference, for four axial stations inside the rotor and five spanwise positions.

($x/c_r = 0.93$), and stator outlet ($x/c_r = 1.87$). For $x/c_r = -0.059$, the velocity is almost constant in the central part of the channel, except for the boundaries of the investigated zone, where lower velocities are found, associated to the rotor blades blockage effect. Note that for $H < 20\%$ the measurements could not be completed because of high noise in the scattered light and the difficulty in introducing proper seeding, as mentioned earlier. The measurements are not shown. For $x/c_r = 0.93$, the rotor wake is identified in the center of the channel as a green lower velocity (around 70 m/s), whereas the velocity providing the major part of the flow rate is at 100 m/s. This lower velocity, bent wake structure ends in a tip clearance vortex, identified by a velocity depression. This vortex originates from the pressure gradient between the pressure side and the suction side of the rotor blade, in the beginning of the rotor chord and is convected to the suction side. Downstream from the blade, the vortex interacts with the rotor blade and goes in the wake to the side corresponding to the pressure side of the blade as mentioned in the preceding section. For $H > 80\%$, because of the carter proximity,

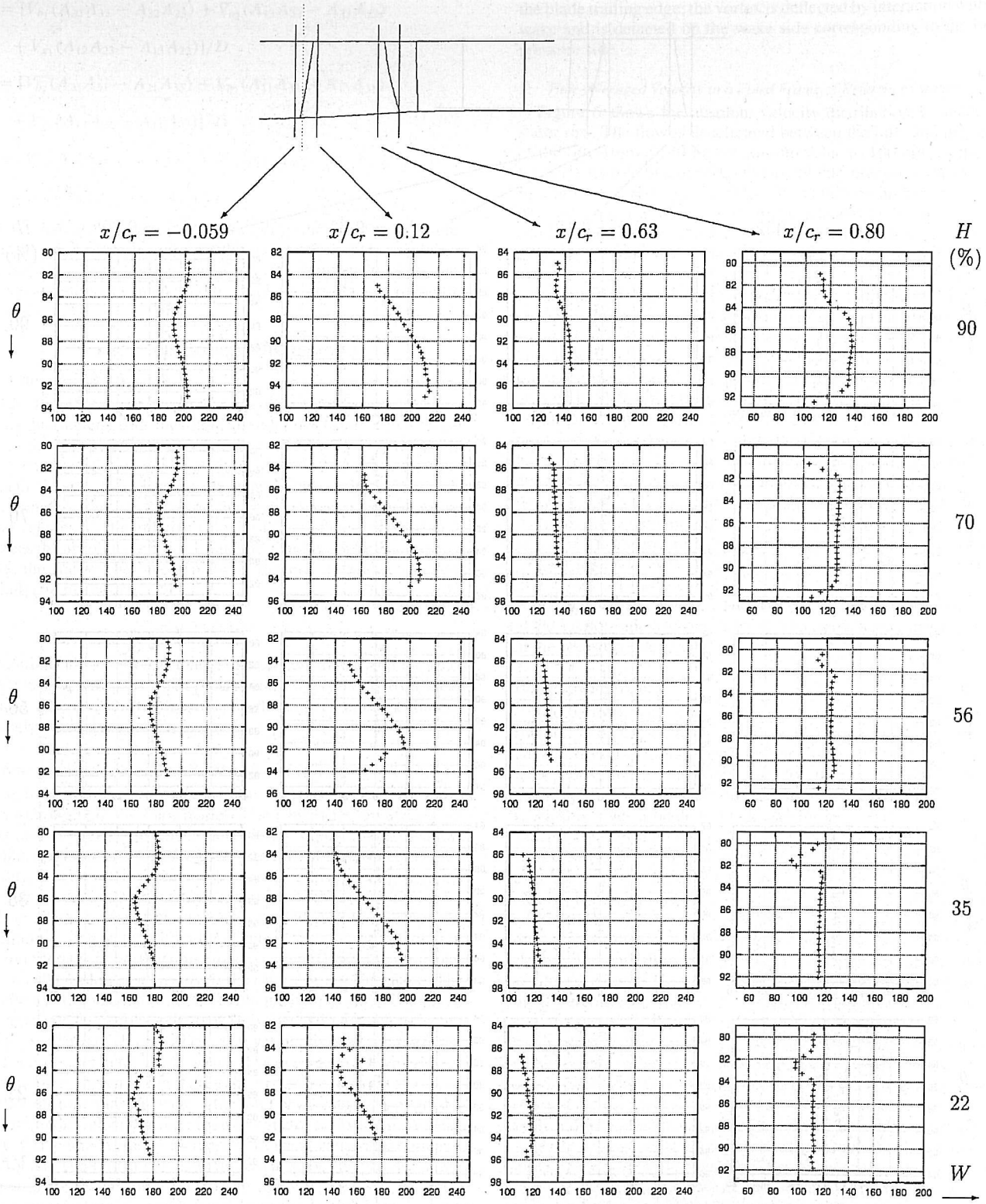

Fig. 5 Tangential distribution (degree) of the relative velocity W (m/s) in a rotating frame of reference, for four axial stations inside the rotor and five spanwise positions.

there is a strong unsteady interaction. It is caused by the main flow and the carter boundary layer on the one hand and the wake and tip clearance vortex on the other hand. Furthermore, the blockages of the stator blades, which are very close of the plane of measurements, are identified as the green stripes at the boundary of the channel. At the stator outlet, $x/c_r = 1.87$, the stator blade wakes can be seen as velocity defects. Inside the channel, the axial velocity is almost uniform, but the rotor wake influence is detected as a bent light blue velocity zone on the right.

The time-dependent tangential velocity is displayed for the same axial measurements planes in Fig. 10. The relative tangential velocity is plotted for the rotor inlet and rotor–stator gap, whereas the absolute velocity is plotted for the stator outlet. For $x/c_r = -0.059$, there is an increase of tangential velocity amplitude from root to tip, with a time-dependent gradient from pressure side to suction side. As for the axial velocity, data below $H = 20\%$ are incorrect and are not given. In the rotor outlet ($x/c_r = 0.93$), the tangential velocity gradient from root to tip is due to a greater amplitude of

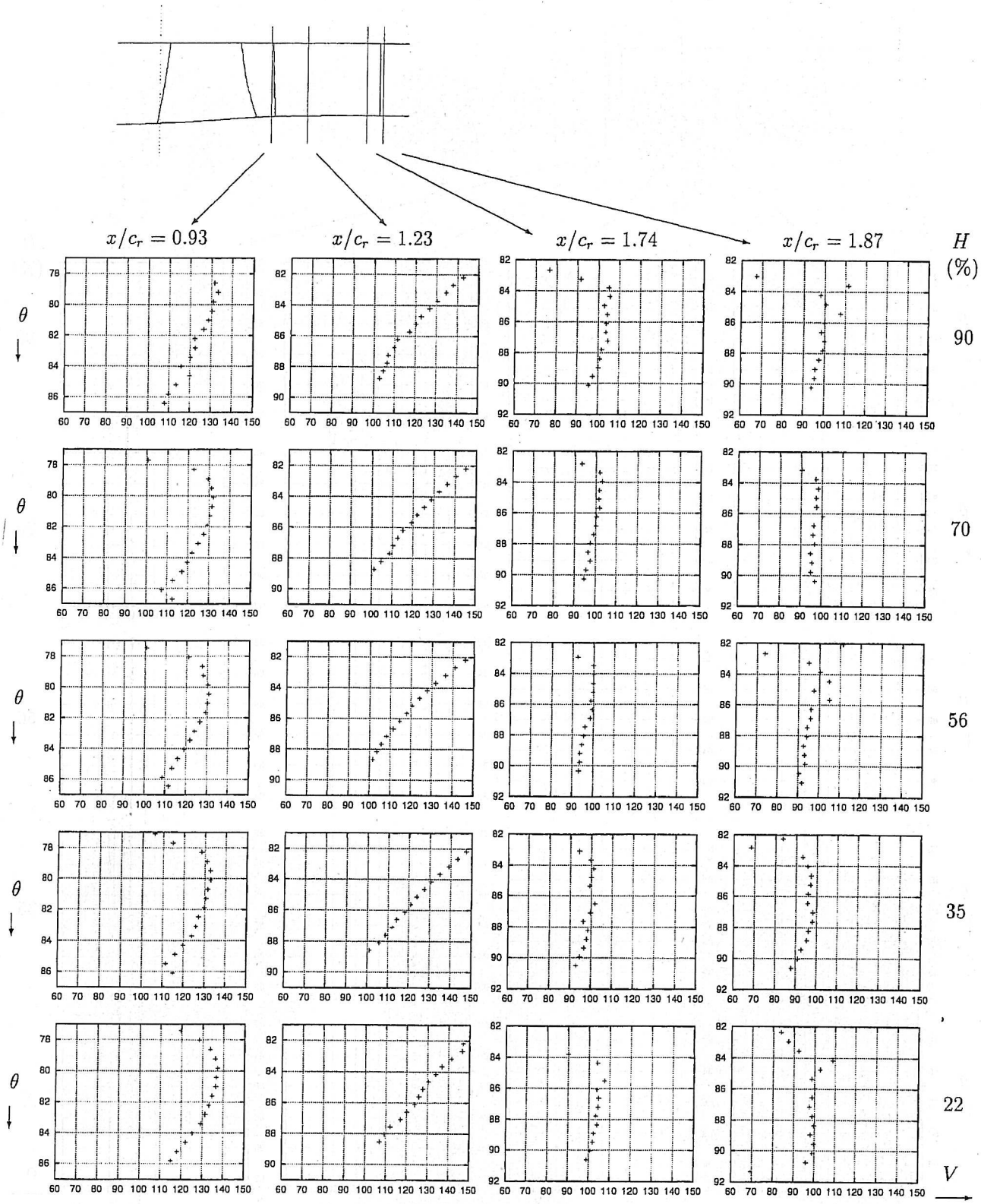

Fig. 6 Tangential distribution (degree) of the absolute velocity V (m/s) in a fixed frame of reference, for four axial stations inside the stator and five spanwise positions.

the entrainment velocity near the casing. In addition, the blade passage creates a time-dependent change in velocity corresponding to the rotor wake. For this phase, it is situated in the middle of the channel. At stator outlet, the absolute tangential velocity is almost zero except in the stator blade wakes, where the flow is deflected. In addition, the rotor wake can be identified as a time-dependent change in the sign of the velocity. For this phase time, it is identified in the upper right corner of the channel.

For a better understanding of the dynamics of the rotor blade wakes, a view in the (x, θ) section for $H = 50\%$ is shown in Fig. 11 for six phases. Three rotor wakes can be identified inside the stator channel; they are pointed out by arrows in their arrival time order for the second time plotted (phase 5). As already mentioned, $\tilde{V}_\theta$ is higher in the wake, and this structure can be seen as a violet–dark blue region in the stator blade inlet. As the rotor wake is swallowed by the stator, the tangential motion decreases. For a given time (for

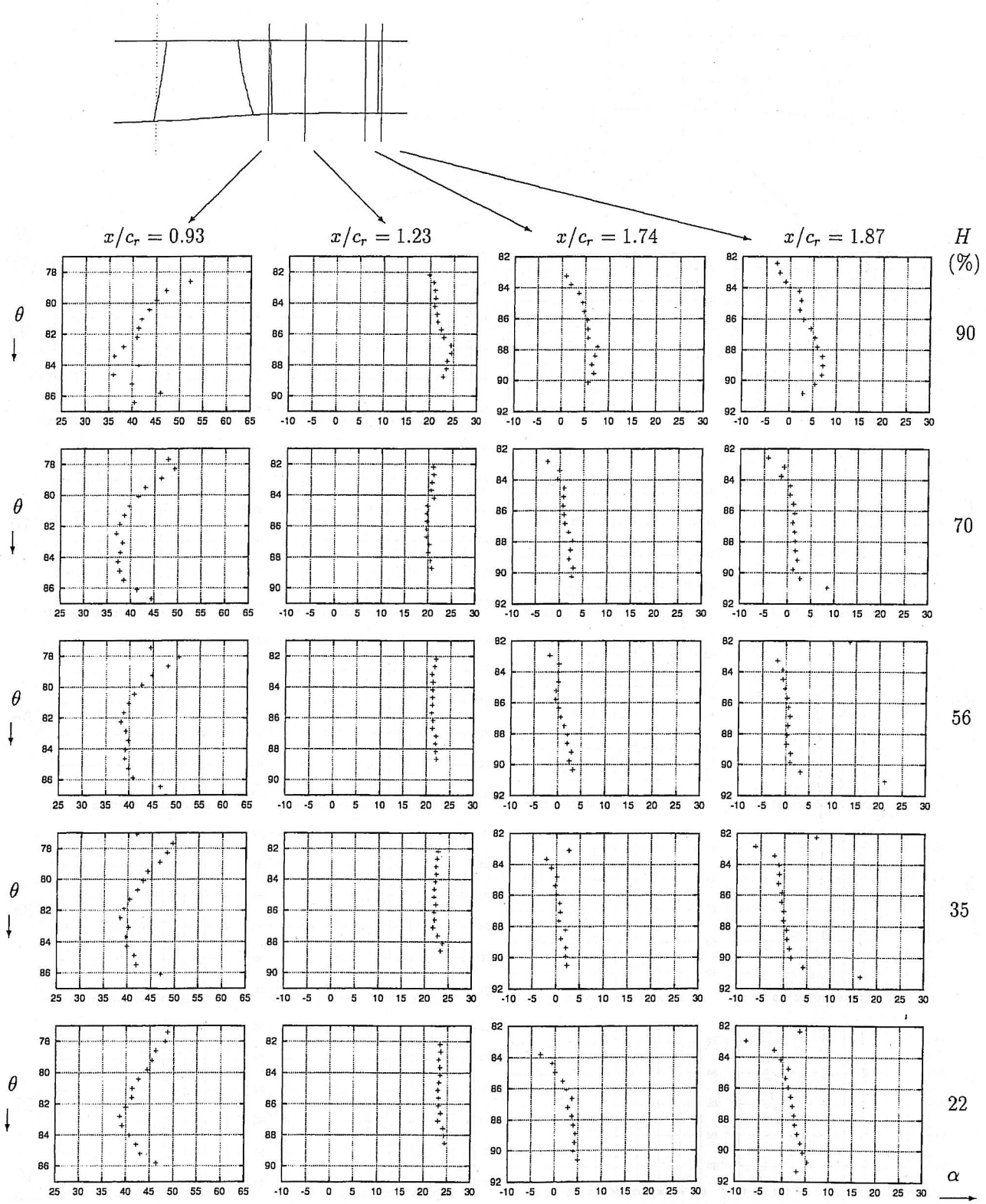

Fig. 7 Tangential distribution (degree) of the absolute radial flow angle α (deg) in a fixed frame of reference, for four axial stations inside the stator and five spanwise positions.

example, phase 9), the three wakes can be identified: The first is upstream from the top blade leading edge, the second is in the middle of the channel, and the third is near the exit. The passing of these wakes induces a periodic variation of the aerodynamic load on the blades. The rotor wakes are cut up by the the stator row, and as a consequence, they interact with the stator blades boundary layers. On the blade pressure side, this interaction is uniform. On the suction side, the wake is interacting with the boundary layer without distortion for around one-third of the blade chord. Downstream, its structure is modified showing a gap between the wake and the blade boundary layer. The rotor wakes are cut up and convected on the suction side faster than on the pressure side. As a consequence, they interfer with the stator wakes, which results in a time-dependent oscillatory flow structure at the outlet. The small red region, associated with a negative velocity, that is present near the stator blade suction side trailing edge is a boundary-layer separation zone. The

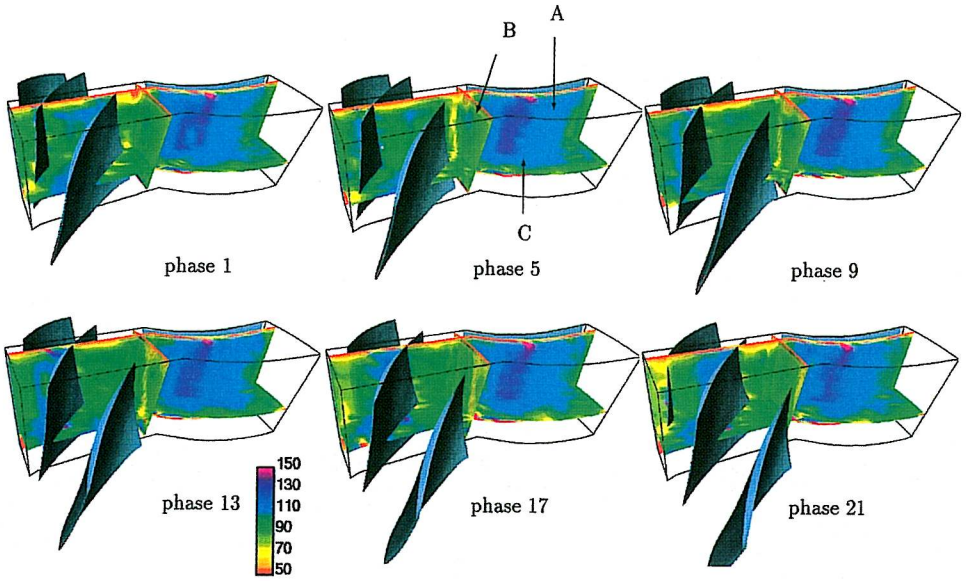

Fig. 8 Distribution of the phase-averaged absolute axial velocity $\tilde{V}_x$ (m/s).

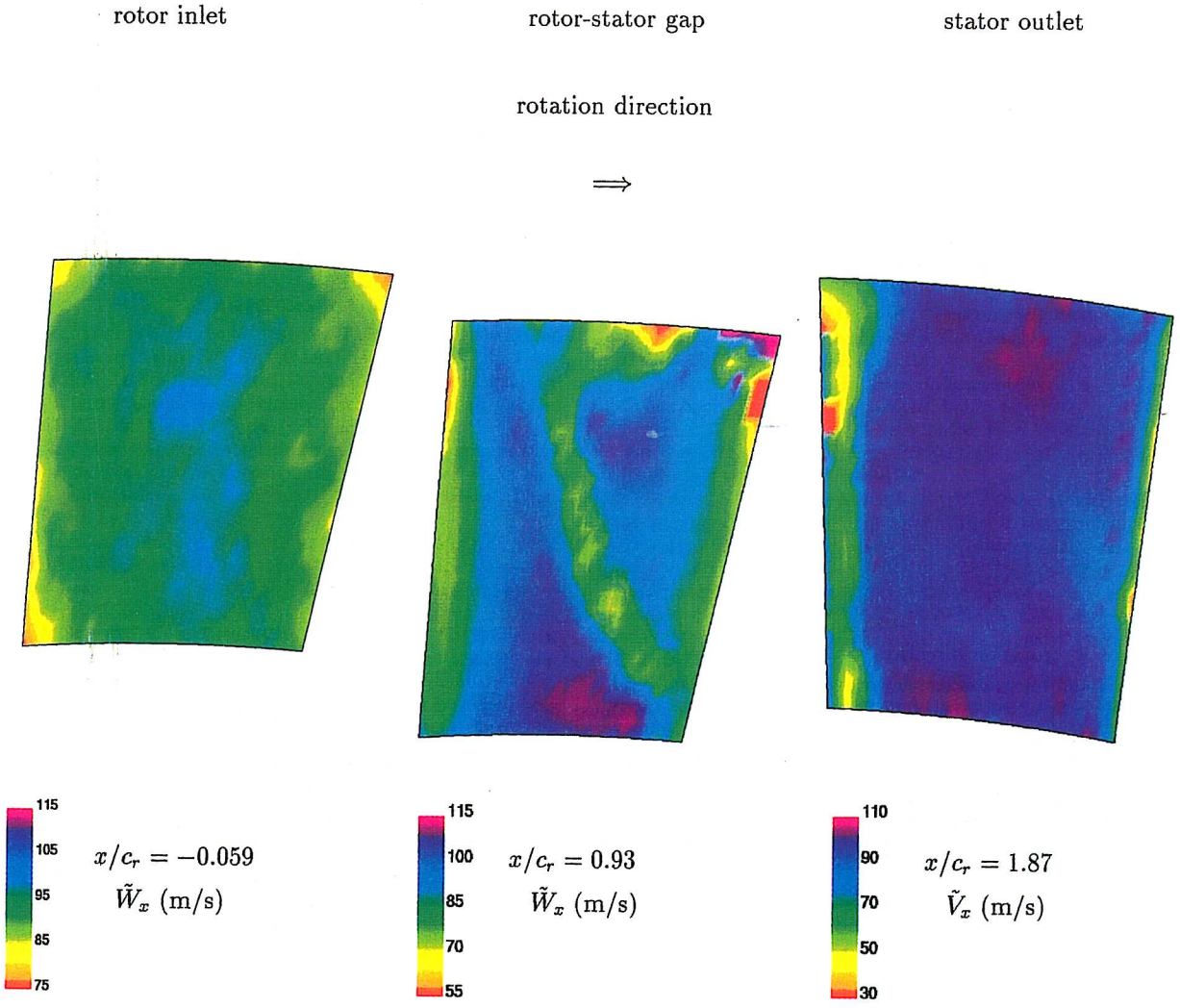

Fig. 9 Distribution of the phase-averaged axial velocity (meter per second) for phase 13.

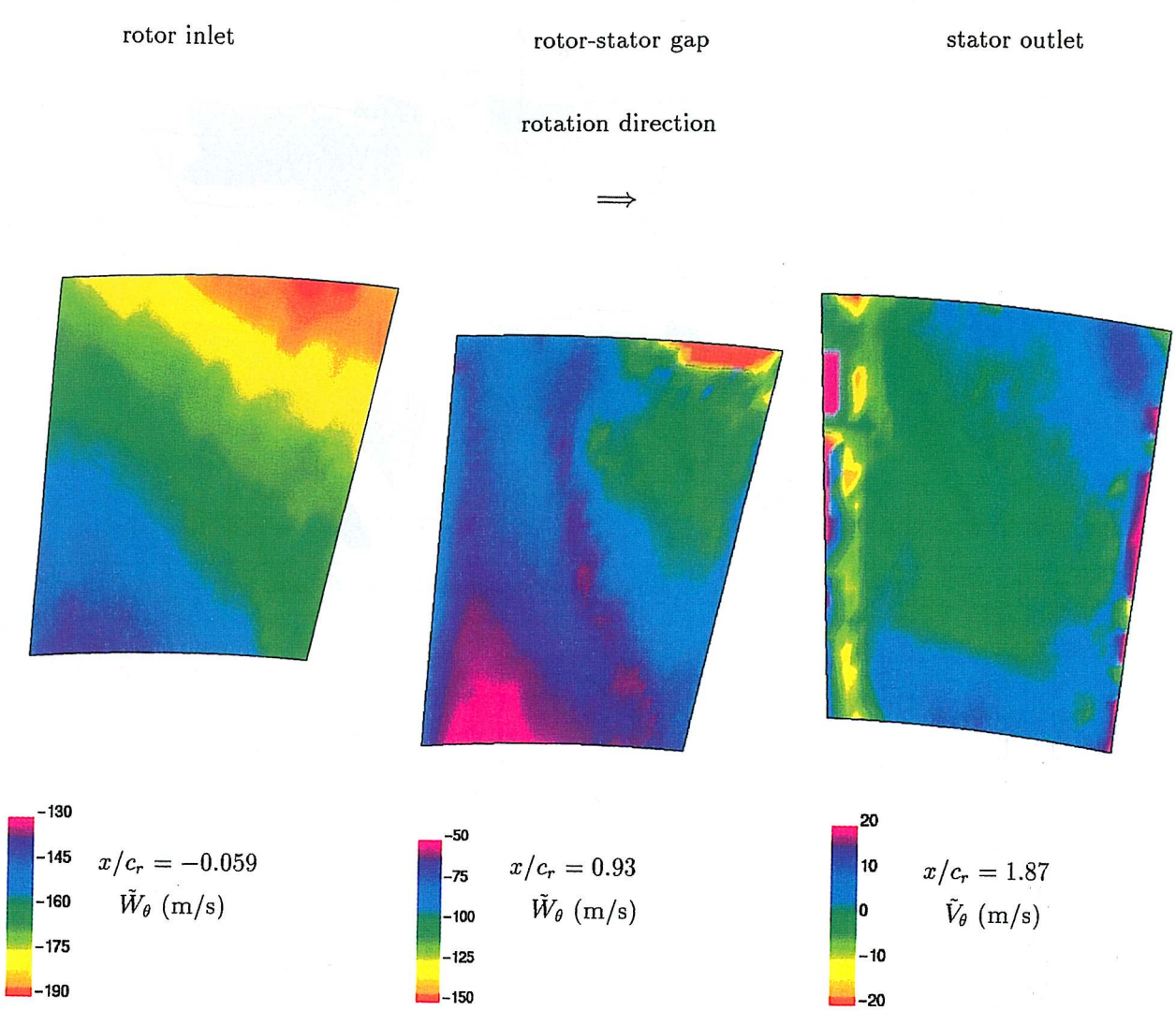

Fig. 10 Distribution of the phase-averaged tangential velocity (meter per second) for phase 13.

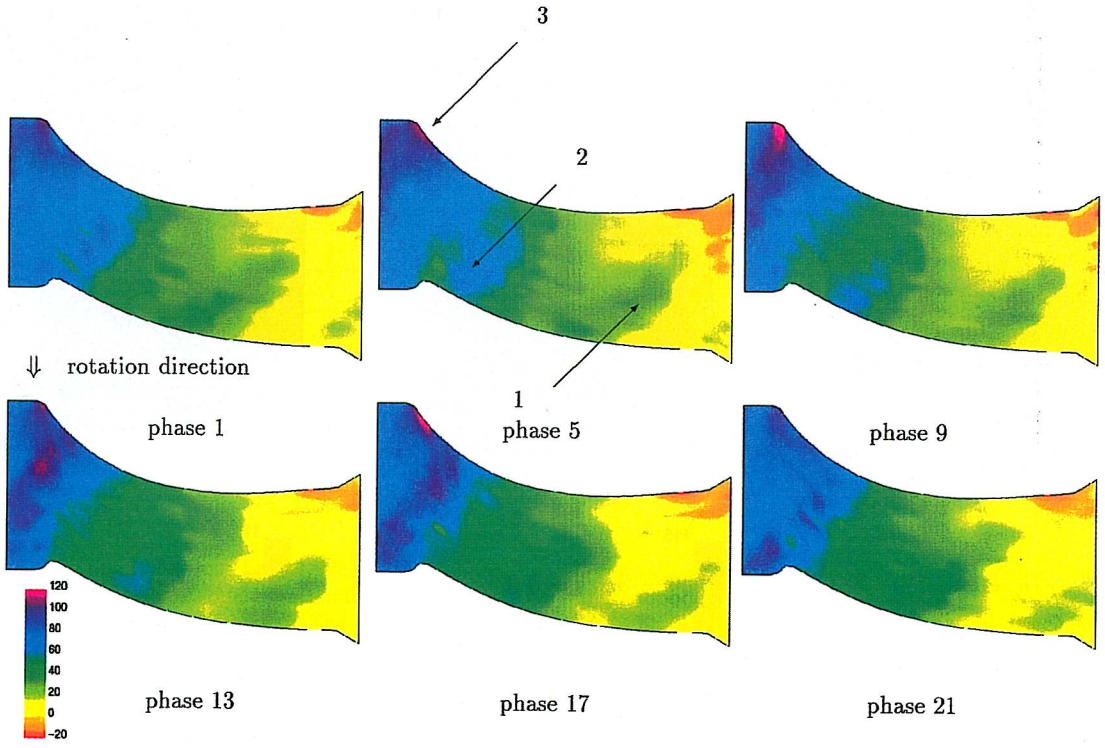

Fig. 11 Distribution of the phase-averaged tangential velocity $\tilde{V}_\theta$ (m/s) for $H = 0.5$ inside the stator.

interaction of this steady zone with the rotor wakes passing increases the phase lag of two successive rotor wakes downstream from the stator blade trailing edge.

IV. Conclusions

A two-component LDA system has been implemented on an axial compressor to study the velocity field. The use of two laser head orientations per point of measurement inside the compressor stage allows the global features of the three-dimensional flow to be obtained with only this laser system. A complete flowfield survey was carried out from the rotor inlet to the stator outlet, and data triggered with the rotor rotation provide phase-averaged results of velocity.

Measurements inside the rotor show the blockage effect caused by the blade leading edge at the inlet, velocity deceleration inside the rotor channel, and the rotor wakes at the exit. The use of BSA is valuable because there is no need to cut the laser beam during the passage of the rotor blades. Inside the stator row, the decay of the flow angle α from the inlet to the outlet is measured.

The phase-averaged three-dimensional view of velocity field over a rotor blade channel permits the observation of the main time-dependent flow characteristics. Casing boundary layers and rotor tip clearance vortices are identified at the rotor outlet. The tip clearance vortex created by pressure gradient on the rotor blade sides is deflected by interaction with the wake and detected in the interrow gap. The rotor wake is cut up by the stator and can be identified as far as the outlet. For a given time, the wakes of three successive blades are observed inside the stator blade to blade channel. The interaction of these wakes with the blade boundary layers generates strong three-dimensional unsteady effects, which are associated with time-dependent aerodynamic loads on the stator blade.

Acknowledgments

The support of the Région Ile de France through a SESAME grant is acknowledged. This work is a part of the Turbo-3D project of the Laboratoire d'Énergétique et de Mécanique des Fluides Interne, Université Pierre et Marie Curie, Paris 6, partially supported by the Société Nationale d'Études et de Construction de Moteurs d'Aviation, Turboméca, Électricité de France and the Centre National de la Recherche Scientifique. The technical assistance of J. P. Dalac and R. Pidoux is gratefully acknowledged. The authors are listed alphabetically.

References

[1]Schodl, R., "Laser-Two-Focus Velocimetry," *Advanced Instrumentation for Aero Engine Components*, CP-399, AGARD, 1986, pp. 7.1–7.31.

[2]Beversdorff, M., Hein, O., and Schodl, R., "An L2F-Measurement Device with Image Rotator Prism for Flow Velocity Analysis in Rotating Coolant Channels," CP-527, AGARD, 1993, pp. 16.1–16.7.

[3]Ottavy, X., "Mesures par anémométrie laser dans un compresseur axial transsonique–Étude des structures instationnaires périodiques," Ph.D. Thesis, No. 99–25, Laboratoire de Mécanique des Fluides et d'Acoustique, École Centrale de Lyon, Lyon, France, May 1999.

[4]Förster, W., Schodl, R., and Rijmenants, E., "Design and Experimental Verification of 3D Velocimeters Based on the L2F Technique," *5th International Symposium on Applications of Laser Techniques to Fluid Mechanics*, Lisbon, Portugal, 1990.

[5]Maass, M., Förster, W., and Thiele, P., "Unsteady Flow Experiment at the Exit of a Ducted Propfan Rotor," *30th AIAA/ASME/SAE/ASEE Joint Propulsion Conference*, Indianapolis, IN, 1994.

[6]Ardey, S., Fottner, L., Beversdorff, M., and Weyer, H., "Laser Two Focus Measurements on a Turbine Cascade with Leading Edge Film Cooling," *90th Symposium of Propulsion and Energetics Panel on Advanced Non-Intrusive Instrumentation for Propulsive Engines*, AGARD, Brussel, Belgium, 1997.

[7]Beversdorff, M., Matziol, L., and Blaha, C., "Application of 3D Laser Two Focus Velocimetry in Turbomachine Investigations," *90th Symposium of Propulsion and Energetics Panel on Advanced Non-Intrusive Instrumentation for Propulsive Engines*, AGARD, Brussel, Belgium, 1997.

[8]Charpenel, S., "Caractérisation d'une technique d'anémométrie laser bipoint tridimensionnelle L2F-3D pour l'analyse de l'écoulement dans un compresseur axial basse-vitesse," Ph.D. Thesis, No. 98-17, Laboratoire de Mécanique des Fluides et d'Acoustique, École Centrale de Lyon, Lyon, France, April 1998.

[9]McLean, C., and Camci, C., "Analysis and Quantification of a Solid-State Laser Doppler Anemometer," *AIAA Journal*, Vol. 33, No. 10, 1995, pp. 1880–1887.

[10]Fraser, R., Pack, J., and Santavicca, D. A., "An LDV System for Turbulence Length Scale Measurements," *Experiments in Fluids*, Vol. 4, 1986, pp. 150–152.

[11]Stephanini, J., Menon, R., Elena, M., and Deleuze, J., "Impact du traitement du signal sur les mesures de vélocimétrie laser Doppler," *5ème Congrès Francophone de Vélocimétrie Laser*, Association Francophone de Vélocimétrie Laser, Rouen, France, Sept. 1996, pp. A5.1–A5.3.

[12]Gallus, H. E., Zeschky, J., and Hah, C., "Endwall and Unsteady Flow Phenomena in an Axial Turbine Stage," *Journal of Turbomachinery*, Vol. 117, Oct. 1995, pp. 562–570.

[13]Walraevens, R. E., Gallus, H. E., Jung, A. R., Mayer, J. F., and Stetter, H., "Experimental and Computational Study of the Unsteady Flow in a 1.5 Stage Axial Turbine with Emphasis on the Secondary Flow in the Second Stator," *International Gas Turbine and Aeroengine Congress and Exhibition*, American Society of Mechanical Engineers, Stockholm, Sweden, June 1998.

[14]Zaccaria, M., Ristic, D., and Lakshminarayana, B., "Three-Dimensional Flowfield in a Turbine Nozzle Passage," *Journal of Propulsion and Power*, Vol. 12, No. 5, 1996, pp. 974–983.

[15]Ristic, D., Lakshminarayana, B., and Chu, S., "Three-Dimensional Flowfield Downstream of an Axial-Flow Turbine Rotor," *Journal of Propulsion and Power*, Vol. 15, No. 2, 1999, pp. 334–344.

[16]Chesnakas, C. J., and Dancey, C. L., "Three-Component Measurements in an Axial-Flow Compressor," *Journal of Propulsion*, Vol. 6, No. 4, 1990, pp. 474–481.

[17]Camp, T. R., and Shin, H. W., "Turbulence Intensity and Length Scale Measurements in Multistage Compressors," *Journal of Turbomachinery*, Vol. 117, Jan. 1995, pp. 38–46.

[18]Murthy, K. N. S., and Lakshminarayana, B., "Laser Doppler Velocimeter Measurement in the Tip Region of a Compressor Rotor," *AIAA Journal*, Vol. 24, No. 5, 1986, pp. 474–481.

[19]Stauter, R. C., "Measurement of the Three-Dimensional Tip Region Flow Field in an Axial Compressor," *Journal of Turbomachinery*, Vol. 115, July 1993, pp. 468–476.

[20]Belhabib, M., and Miton, H., "Experimental Analysis of Unsteady Blade Rows Interaction in a Multistage Turbomachine," *Journal de Physique III*, Vol. 5, Dec. 1995, pp. 2003–2028.

[21]Blidi, S., and Miton, H., "Basic Instrumentation of a Low Speed Axial Compressor," *Journal de Physique III*, Vol. 5, July 1995, pp. 919–924.

[22]Blidi, S., and Miton, H., "Use of the Hot Wire Anemometry for Velocity and Temperature Measurements in a Turbomachine," *Journal de Physique III*, Vol. 5, Oct. 1995, pp. 1513–1535.

[23]Miton, H., Belhabib, M., and Kus, U., "Experimental and Numerical Investigation of Unsteady Flow Properties in a Stator of Multistage Flow Compressor," *85th Symposium on Loss Mechanisms and Unsteady Flows in Turbomachines*, CP-571, AGARD, 1996, pp. 20.1–20.17.

[24]Pradère, T., "Contribution au développement de la vélocimétrie laser Doppler dans les turbomachines," Ph.D. Thesis, Laboratoire d'Énergétique et de Mécanique des Fluids Interne, Univ. Pierre et Marie Curie, Paris, France, Dec. 1998.

[25]Strazisar, A. J., "Laser Fringe Anemometry for Aero Engine Components," *Advanced Instrumentation for Aero Engine Components*, CP-399, AGARD, 1986, pp. 6.1–6.32.